PET image reconstruction: mean, variance, and optimal minimax criterion



2015 J. Phys. D: Appl. Phys. 48 155401

(http://iopscience.iop.org/0022-3727/48/15/155401)

IOP Publishing Journal of Physics D: Applied Physics

J. Phys. D: Appl. Phys. **48** (2015) 155401 (11pp) doi:10.1088/0022-3727/48/15/155401

# PET image reconstruction: mean, variance, and optimal minimax criterion

**Huafeng Liu[1], Fei Gao[2], Min Guo[1], Liying Xue[3], Jing Nie[4] and Pengcheng Shi[2]**

[1] State Key Laboratory of Modern Optical Instrumentation, Department of Optical Engineering, Zhejiang University, Hangzhou, People's Republic of China
[2] B. Thomas Golisano College of Computing and Information Sciences, Rochester Institute of Technology, Rochester, NY 14623, USA
[3] Yumen Oilfield Hospital, PetroChina Yumen Oilfield Company, Jiuquan, Gansu, People's Republic of China
[4] International Cooperation Auditing Department of China National Petroleum Auditing Service Center, Fenghe Building, Taiyang Gong Street 23, Beijing, People's Republic of China

E-mail: liuhf@zju.edu.cn

Received 23 October 2014, revised 9 February 2015
Accepted for publication 19 February 2015
Published 20 March 2015


**Abstract**

Given the noise nature of positron emission tomography (PET) measurements, it is critical to know the image quality and reliability as well as expected radioactivity map (mean image) for both qualitative interpretation and quantitative analysis. While existing efforts have often been devoted to providing only the reconstructed mean image, we present a unified framework for joint estimation of the mean and corresponding variance of the radioactivity map based on an efficient optimal min–max criterion. The proposed framework formulates the PET image reconstruction problem to be a transformation from system uncertainties to estimation errors, where the minimax criterion is adopted to minimize the estimation errors with possibly maximized system uncertainties. The estimation errors, in the form of a covariance matrix, express the measurement uncertainties in a complete way. The framework is then optimized by ∞-norm optimization and solved with the corresponding $H_\infty$ filter. Unlike conventional statistical reconstruction algorithms, that rely on the statistical modeling methods of the measurement data or noise, the proposed joint estimation stands from the point of view of signal energies and can handle from imperfect statistical assumptions to even no *a priori* statistical assumptions. The performance and accuracy of reconstructed mean and variance images are validated using Monte Carlo simulations. Experiments on phantom scans with a small animal PET scanner and real patient scans are also conducted for assessment of clinical potential.

Keywords: image reconstruction, variance, minimax criterion, H infinity filter, positron emission tomography

(Some figures may appear in colour only in the online journal)

## 1. Introduction

Positron emission tomography (PET) as a biomedical research technique and clinical diagnostic procedure is one of the most important applications in nuclear medical imaging devices. In the past three decades, there has been a significant advancement in PET image reconstruction methods, but several challenges remain [1–3].

PET image reconstruction usually involves recovering the unknown spatial–temporal radioactivity distribution from the acquired annihilation photon pairs. Until now the most attractive methods have been statistical reconstruction algorithms, which are well suited to modeling of the acquisition effects such as positron range, spatially varying spatial resolution, and non-uniform attenuation [4–7]. These effects are included as components in the least square (LS) or maximization

 

likelihood (ML) objective functions for image reconstructions, which are derived from *a priori* statistical knowledge assumptions of the noisy measurement data. LS minimizing criteria measure the goodness of fit between the predicted data by means of modeling the acquisition process and the measured data, and derived approaches include LS–conjugated gradient (LS-CG) [8], expectation maximization–LS (EM-LS) [9], penalized weighted least square (PWLS) [10]and so on. ML criteria maximize the products of Poisson probabilities, which serve as statistical models of the PET measurements, including the originated ML—EM [11–13], shifted Poisson–EM (EMSP) algorithm for random pre-corrected data [14–16], accelerated EM algorithm–ordered subset EM (OSEM) [17, 18] and various maximum a posteriori (MAP) strategies by imposing image priors (e.g. Gibbs prior) and different independent priors (e.g. Gaussian prior, Gamma prior) [19–23]. Tong *et al* introduced a state space solution framework with $H_\infty$ optimization, but still based on a predefined compartment model [24].

However, in PET emission scans, the measurement data are unfortunately contaminated by random coincidence events and scatter coincidence events and affected by attenuation, detector efficiency, energy resolution, time resolution, etc [25–28]. Generally, the PET measurement data $y$ are first processed by various data corrections (including random correction, normalization correction, deadtime correction, scatter correction and attenuation correction sequentially), then the output $y_{\text{rndsa}}$ (the subscript means the corrections applied) is used for image reconstruction. $y$ is Poisson distributed; however, the above data processing procedure makes PET measurement data after corrections $y_{\text{rndsa}}$ follow a more complicated distribution rather than a single Gaussian/Poisson distribution or their simple combinations. Various data corrections make it nearly impossible to obtain an exact *a priori* statistical model of measurement data or noises as the statistical reconstruction algorithms demand. Additionally, due to the individual differences in patients, there will be unavoidable mismatch between general modeling and a specific patient. All the aforementioned uncertainties will limit the accuracy of PET image reconstruction and lead to suboptimal results. Furthermore, with the development of a full 3D PET scanner and in 3D acquisition mode [29–34], the uncertainties are more complicated than in 2D acquisition mode. For example, the uncertainties in time resolution and detector efficiency will be different due to development in scintillators and photomultiplier tubes in newer systems [35]. As a result, PET image reconstruction becomes an extremely complicated problem.

For any image reconstruction method, analytical or statistical, the expected image $\hat{x}$ is reconstructed by solving a certain *inverse problem* as some explicit or implicit function of the measurement data $y_{\text{rndsa}}$, say $\hat{x} = R(y_{\text{rndsa}})$. The noise in the measurement data propagates, and eventually leads to accuracy problems or uncertainty in reconstructed images. For a fixed radioactivity distribution $x$, measurement data $y_{\text{rndsa}}$ can be described as a random variable with a probability density function conditioned on $x$. Then $\hat{x}$ should also be a random variable with a probability density function conditioned on $x$. Therefore, noise in the reconstructed images can be characterized by the covariance matrix $\text{Cov}(\hat{x})$ or its diagonal entries, namely, variance. Apart from the reconstructed image, quantitative estimation of image variance and uncertainty is also critical in many cases of theoretical study and clinical applications. Practical applications of such quantitative analysis have been achieved to optimize scanner systems [36, 37] as well as controlling iteration number and designing regularization functions or parameters [19, 38, 39].

While it is relatively straightforward to compute variance for linear analytical approaches such as filtered backprojection [40, 41], the situation in the case of iterative methods is further complicated. Several groups have been dedicated to developing closed-form expressions for different iterative algorithms over the last two decades. These efforts fall into two main categories: iteration-based and fixed-point analysis. The iteration-based analysis techniques calculate variances as functions of iteration number and have been successfully used in MLEM [42], OSL-MAP-EM [43] and unregularized block iterative algorithms [44].This category is attractive for algorithms that are terminated before convergence, as is common practice for the EM algorithm and its ordered-subset variants. The final results calculated for this category are influenced by the iterative algorithm used, the initial state, and the iteration number. Alternatively, the fixed-point category [19, 45] assumes that the iterative algorithm has converged at a unique and stable solution, allowing us to compute image statistics, independent of the iteration number. These two categories are actually complementary, and more general frameworks [46, 47] considering both iteration-based and fixed-point analysis were later developed for a range of reconstruction algorithms. However, the above process of variance estimation employs a derived framework apart from that used for image reconstruction. As is often the case, the estimation of image variance is carried out after image reconstruction.

In this paper, we try to perform both mean and variance image estimation from the viewpoint of signal energies instead of only statistical assumptions, which makes the framework able to handle from imperfect statistical assumptions to even no *a priori* statistical assumptions. Unlike conventional approximate expressions, the variance is calculated along with the image reconstruction in one unified framework. The data errors during PET data acquisition are used as input and an estimation of errors between the estimations of the imaging object and its expected values as output. Therefore, the minimax criterion can be adopted to minimize the estimation errors with possibly maximized data errors. A system gain is calculated based on the energies of errors, which makes the criterion robust to complicated statistical properties of measurement data and modeling uncertainties [48–50]. The proposed minimax criterion can incorporate all possible uncertainties into the objective function based on the $\infty$-norm of system gains [51, 52]. Correspondingly, in this paper, we choose $H_\infty$ reconstruction as the optimization for the $\infty$-norm minimax objective function [52, 53]. $H_\infty$ reconstructions can minimize the expectation errors and help to reduce the variance errors with possibly maximized data errors and modeling uncertainties in the system. The performance and accuracy of reconstructed mean and variance images are first validated

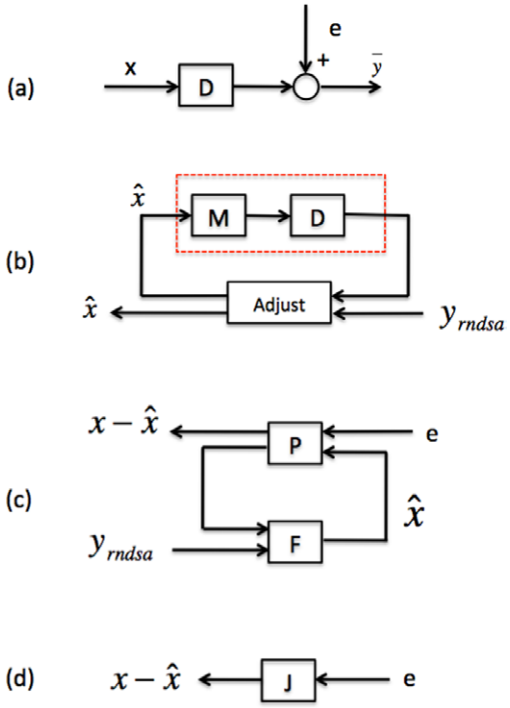


**Figure 1.** Block diagrams. (*a*) PET data acquisition; (*b*) statistical model based iterative PET reconstruction; (*c*) designed system for PET image reconstruction; (*d*) simplified block diagram (black box) of (*c*).

using Monte Carlo simulations. Our method can obtain improved reconstruction results over conventional statistical reconstruction algorithms and shows advantages in cases that contain complicated noise distribution. Experiments on phantom scans by a small animal PET scanner and real patient scans are also conducted for assessment of clinical potentials.

## 2. Theory

### *2.1. Mathematical modeling and statistical formulation of PET image reconstruction*

The goal of mathematical modeling of data acquisition is to describe the transforms from spatial distributions of imaging objects to projection distributions on detector pairs in the PET system. Denoting the spatial distribution of the imaging object by a set of spatial variables $x = \{x_i | i = 1 \cdots n\} \in \mathbb{R}^n$, where $n$ is the total number of voxels, and the expected values (means) of projection bins by $\bar{y} = \{\bar{y}_j | j = 1 \cdots k\} \in \mathbb{R}^k$, where $k$ is the total number of bins, a mathematical expression of the transform can be obtained:

$$\bar{y} = Dx + \bar{e} \tag{1}$$

where $D$ is the system response model giving the probability matrix of mapping the transform from $x$ to $\bar{y}$, and $\bar{e}$ is the means of background noises. A block diagram of the above procedure is shown in figure 1(*a*).

The problem of PET image reconstruction is to find an estimation of the imaging object $\hat{x}$ from the corrected measurement data $y_{\text{rndsa}}$. Since image reconstruction is an ill-posed inverse problem, one solution is to apply statistical models of measurement data as regularizations. A simple block diagram of statistical formulation is shown in figure 1(*b*): the statistical properties of system noises or measurement data are first modeled based on certain statistical distributions (Gaussian, Poisson, their combination or other derivations) in block $M$, then inputted into system block $D$; the system output is generated and compared with corrected measurement data $y_{\text{rndsa}}$ based on the predefined criteria; when convergence is achieved, estimations of the imaging object $\hat{x}$ will be obtained. Three major basic criteria (LS, ML and MAP) are listed as follows.

$$\hat{x} = \arg\min_x \| y_{\text{rndsa}} - Dx \|_2^2 \tag{2}$$

$$\hat{x} = \arg\max_x p(y_{\text{rndsa}}|x) \tag{3}$$

$$\hat{x} = \arg\max_x p(x|y_{\text{rndsa}}) = \frac{p(x, y_{\text{rndsa}})}{p(y_{\text{rndsa}})} = \frac{p(y_{\text{rndsa}} \mid x)p(x)}{p(y_{\text{rndsa}})} \tag{4}$$

where $p$ represents the probability density, and $p(x, y_{\text{rndsa}})$ is the joint probability density of $x$ and $y_{\text{rndsa}}$. The statistical formulation tries to find an optimized relationship between measurement data $y_{\text{rndsa}}$ and imaging object $x$ (or expected values of projection bins $\bar{y}$) by defining different objective functions. All the above objective functions demonstrate the implied statistical knowledge assumptions on measurement data or noises in mathematical modeling.

### *2.2. Minimax criterion*

As discussed previously, there are mismatches between modeling assumptions and statistical distribution of corrected measurement data; here we introduce the minimax criterion to reconstruct the measurement data $y_{\text{rndsa}}$. As shown in figure 1(*c*), a new block $F$ is designed to reconstruct measurement data $y_{\text{rndsa}}$; the difference between expected values of imaging object $x$ and estimation values $\hat{x}$ is designed as the output of a block $P$ which contains system response $D$ and noise $e$. Because measurement data $y_{\text{rndsa}}$ are constant during image reconstruction, the system can be simplified with an inner loop of block $F$ and $y_{\text{rndsa}}$ incorporated into block $P$ and yield a black box system $J$ as shown in figure 1(*d*). For this system, the minimax criterion can then be applied to minimize the output (estimation errors $x - \hat{x}$) with possibly maximized input (errors and uncertainties $e$) through a transformation system $J$:

$$\hat{x} = \min_{x-\hat{x}} \max_e J \tag{5}$$

In order to solve the minimax function, a proper upper bound of estimation errors must be defined first, which means the transfer function of system $J$ will also be required to have a system gain that conforms to the same predefined upper bound. When the upper bound is defined as $\gamma^2$, the maximum of system gain should satisfy

$$\max \| J \|^2 < \gamma^2. \tag{6}$$

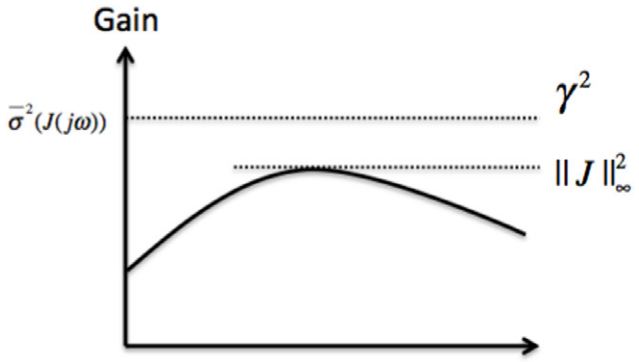


**Figure 2.** Illustration of system gains and predefined upper bound.

Because the ∞-norm of the system can be interpreted as the peak system gain, if the ∞-norm of the system satisfies $\| J \|_\infty^2 < \gamma^2$, then all the system gains will be less than $\gamma^2$, as illustrated in figure 2. Moreover, the ∞-norm of the system gain is an element of the Hardy space, whose members consist of all stable, causal, transf er functions [51]. The continuous form of the ∞-norm $|J|_\infty$ will be

$$\| J \|_\infty^2 = \sup_{\|e\|_2 \neq 0} \frac{\| x - \hat{x} \|_2^2}{\| e \|_2^2} = \sup_\omega \bar{\sigma}^2(J) \tag{7}$$

where sup stands for supremum, and $\bar{\sigma}(J)$ is the maximum singular value of $J$. From equation (7), it is easy to obtain

$$\max \| J \| \leq \| J \|_\infty^2 = \sup_{\|e\|_2 \neq 0} \frac{\| x - \hat{x} \|_2^2}{\| e \|_2^2} < \gamma^2 \tag{8}$$

The problem is transformed from seeking the maximum system gain of $J$ to calculating the ∞-norm of system gain with upper bound $\gamma^2$.

Equation (8) also reflects the meanings of minimax; in order to calculate the inequality, intuitively we can minimize the numerator (estimation errors $x - \hat{x}$) while maximizing the denominator (system disturbance $e$). Then the objective function for our problem will be

$$\min_{x-\hat{x}} \max_{e} \| x - \hat{x} \|_2^2 - \gamma^2 \| e \|_2^2 < 0 \tag{9}$$

Seeking solutions under errors and uncertainties is a difficult problem. By introducing the ∞-norm of system gain, solutions with peak system gain will perform well under any circumstance and make the problem globally optimized. Furthermore, the minimax criterion allows one to identify a robust solution that has the best worst-case performance. The robustness of the estimator arises from the fact that it yields an energy gain less than $\gamma^2$ for all bounded energy disturbances no matter what they are, and dependence on accurate statistical modeling is no longer needed.

### 2.3. A general PET reconstruction framework

PET images reflect the concentration and metabolism of radiotracers *in vivo*, and the physical natures of radiotracer metabolism in organs or tissues can be adopted as constraints. We have successfully applied the natural decay of the radiotracer [54] and compartment models [24, 55] as constraints. Here we build a more general framework, which is able to be free of constraints. As stated in the above papers, the iterative PET image reconstruction can be presented as

$$x(m+1) = \hat{x}(m) + v(m) \tag{10}$$

where $m$ represents the current iteration step, $\hat{x}$ is the estimation of $x$ and $v$ is the tiny possible disturbances, which also accounts for the uncertainties between general modeling and an individual patient. More generally, the above equation can be extended to be

$$x(m+1) = H(m)\hat{x}(m) + v(m) \tag{11}$$

Here, $H$ is the updating term derived from constraints if available.

Correspondingly, the PET measurement equation for each iteration step will be

$$y_{\text{rndsa}} = Dx(m) + e(m) \tag{12}$$

Furthermore, the iterative reconstruction algorithm may also be affected by its initialization selection (especially the convergence speed), so the initialization of $x$ is also considered as $x$ (0) in our objective function. Along with the state transition uncertainties $v$ in equation (11) and the measurement data error $e$ in equation (12), the ∞-norm of the system will be extended from equation (8) to be

$$\| J \|_\infty^2 = \sup \frac{\sum_m \| x(m) - \hat{x}(m) \|_{Z(m)}^2}{\| x(0) - \hat{x}(0) \|_{p_0^{-1}}^2 + \sum_m (\| v(m) \|_{V(m)^{-1}}^2 + \| e(m) \|_{E(m)^{-1}}^2)} \tag{13}$$

$Z(m)$, $p_0$, $V(m)$ and $E(m)$ are the weighting matrixes at iteration $m$ to make the criterion more extensible. After defining the upper bound $\gamma^2$, the final objective function of the minimax criterion for PET image reconstruction can be derived based on equations (9) and (13), which minimizes the estimation errors $x - \hat{x}$ with possibly maximized initial uncertainty $x(0) - \hat{x}(0)$, measurement uncertainty $e$ and state transition uncertainty $v$:

$$\begin{aligned} \min_{z(m)-\hat{z}(m)} \max_{v,e,x(0)-\hat{x}(0)} \| J \|^2 = & \sum_m \| x(m) - \hat{x}(m) \|_{Z(m)}^2 \\ & - \gamma^2 \| x(0) - \hat{x}(0) \|_{p_0^{-1}}^2 \\ & - \gamma^2 \sum_m (\| v(m) \|_{V(m)^{-1}}^2 \\ & + \| e(m) \|_{E(m)^{-1}}^2) \end{aligned} \tag{14}$$

Here the final objective function of the minimax criterion for PET image reconstruction is established without any assumptions of statistical distributions of measurement data and uncertainties. The system gain is calculated based on the energies of uncertainties.

### 2.4. $H_\infty$ optimization

There are many methods that can be adopted to solve the above objective function; here we choose the well validated $H_\infty$ filter to optimize this ∞-norm problem. Many papers have

been published to show the robustness and optimization of $H_\infty$ filter [51, 53]. Here a specific $H_\infty$ filter has been derived based on equation (14). The $H_\infty$ filter represents a typical minimax problem where the worst situation is first induced by the errors and uncertainties, then the estimator is introduced for improvement; in other words, the $H_\infty$ filter is in fact a two-person game between the external disturbances and the estimator. This solution is just like optimization using a game theoretic algorithm which can be implemented through recursive updating of the filter gain $K(m)$, the Riccati difference equation solution $P(m)$, and the state estimates $\hat{x}(m)$ as follows:

$$\bar{P}(m) = P(m) + V(m) \tag{15}$$

$$S(m) = (I - \gamma^{-2}Z(m)\bar{P}(m) + D^{\mathrm{T}}E(m)^{-1}D\bar{P}(m))^{-1} \tag{16}$$

$$K(m) = H(m)\bar{P}(m)S(m)D^{\mathrm{T}}E(m)^{-1} \tag{17}$$

$$\hat{x}(m+1) = H(m)\hat{x}(m) + K(m)(y_{\mathrm{rndsa}} - D\hat{x}(m)) \tag{18}$$

$$\begin{aligned} P(m+1) &= H(m)\overline{P}(m)S(m)H(m)^{\mathrm{T}} \\ P(0) &= p_0 \end{aligned} \tag{19}$$

where $H_\infty$ gain $K(m)$ indicates the system gain (correspondingly shows the convergence of the estimation). Convergent results will be obtained when the gain $K(m)$ goes steadily. $m$ still represents the number of iterations. From the above solution procedure, it can be noticed that the $H_2$ norm filter for this objective function is just the widely used Kalman filter. Detailed proofs of the above solution can be found in [53].

### 2.5. Variance estimation

It has been well proved that the Kalman filter gives an unbiased estimate. In the limiting case, if the parameter $\gamma$ approaches $\infty$, the $H_\infty$ filter approaches the Kalman filter [53]. When a relatively large $\gamma$ is employed, the $H_\infty$ filter can also be approximately regarded as an unbiased estimate. Thus the true image $x$ can be a reasonable approximation of the mean image $E(\hat{x})$:

$$E(\hat{x}) \approx x. \tag{20}$$

Then the covariance matrix will be

$$\begin{aligned} \mathrm{Cov}(\hat{x}) &= E((\hat{x} - E(\hat{x}))((\hat{x} - E(\hat{x}))^{\mathrm{T}}) \\ &\approx E((\hat{x} - x)((\hat{x} - x)^{\mathrm{T}}) = P \end{aligned} \tag{21}$$

where the right-hand side of the approximately equal sign is defined as the estimate error covariance in the $H_\infty$ filter in section 2.4. Hence the covariance matrix of the estimated image $\mathrm{Cov}(\hat{x})$ is approximated by the estimate error covariance $P$. As the $H_\infty$ filter recursive procedure progresses, both the estimated state $\hat{x}$ and covariance $\mathrm{Cov}(\hat{x})$ can be updated simultaneously, and eventually arrive at convergent results.

Along with the mean of the estimated image $E(\hat{x})$, the covariance matrix $\mathrm{Cov}(\hat{x})$ should in principle suffice as a complete statistical noise description set of the reconstructed state and measurement uncertainties. The diagonal entries of this matrix represent the ensemble variance of individual voxels of the estimated state. The off-diagonal entries stand for covariance of two voxels.

### 2.6. Computation issues

The design of the $H_\infty$ filter consists of choosing the weighting matrices $Z$, $E$, $V$, $p_0$ and the performance bound $\gamma^2$ [56]. When there are accurate modelings of some effects of PET acquisition, $E$, $V$, and $p_0$ can be initialized by corresponding covariance matrices of random variables from the models. If there are no models or one does not want to use current models, $E$, $V$, and $p_0$ can be simply initialized by identity matrixes. Moreover, since we generally assume the estimation results after convergence are just what we desired, $Z$ will be initialized by the identity matrix. $\gamma^2$ is the predefined upper bound of performance. Theoretically, the smaller the $\gamma^2$ value, the smaller the estimation error; however, the selection of $\gamma^2$ must make the Riccati equation have a positive definite solution. So first, we define and iteratively update a residual matrix $R(m+1)^{-1}$ through

$$R(0) = (P(0)^{-1} - \gamma^{-2}Z(0))^{-1} \tag{22}$$

$$\begin{aligned} R(m+1)^{-1} = {} & [H(m)(R(m)^{-1} + D^{\mathrm{T}}E(m)^{-1}D)^{-1}H(m)^{\mathrm{T}} \\ & + V(m)]^{-1} - \gamma^{-2}Z(m) \end{aligned} \tag{23}$$

As a result, the optimal $\gamma$ value can be determined as:

$$\begin{aligned} & [H(m)(R(m)^{-1} + D^{\mathrm{T}}E(m)^{-1}D)^{-1}H(m)^{\mathrm{T}} + V(m)]^{-1} \\ & -\gamma^{-2}Z(m) > 0 \\ & \rightarrow [H(m)(R(m)^{-1} + D^{\mathrm{T}}E(m)^{-1}D)^{-1}H(m)^{\mathrm{T}} \\ & + V(m)]^{-1} > \gamma^{-2}I \\ & \rightarrow \gamma^2 I > H(m)(R(m)^{-1} + D^{\mathrm{T}}E(m)^{-1}D)^{-1}H(m)^{\mathrm{T}} \\ & + V(m) \\ & \rightarrow \gamma^2 > \max\{\mathrm{eig}[H(m)(R(m)^{-1} + D^{\mathrm{T}}E(m)^{-1}D)^{-1}H(m)^{\mathrm{T}} \\ & + V(m)]\} \\ & \rightarrow \gamma = \xi\max\{\mathrm{eig}[H(m)(R(m)^{-1} + D^{\mathrm{T}}E(m)^{-1}D)^{-1}H(m)^{\mathrm{T}} \\ & + V(m)]\}^{0.5} \end{aligned} \tag{24}$$

where $\max\{\mathrm{eig}(A)\}$ denotes the maximum eigenvalue of the matrix $A$, and $\xi$ is a constant larger than 1 to ensure that $\gamma$ is always greater than a certain optimal performance level. If the $\gamma$ value is too close to the optimal performance level, i.e. $\xi \approx 1$, it might lead to numerical errors because the matrix $R(m)$ is now close to a singular matrix.

## 3. Experiments and results

Three groups of experiments are conducted to validate the performance of the proposed minimax reconstruction framework, including a Monte Carlo simulated data set from a Zubal thorax phantom, experiments with a Derenzo phantom with a small animal PET scanner and real patient scans with a commercial whole body PET scanner.

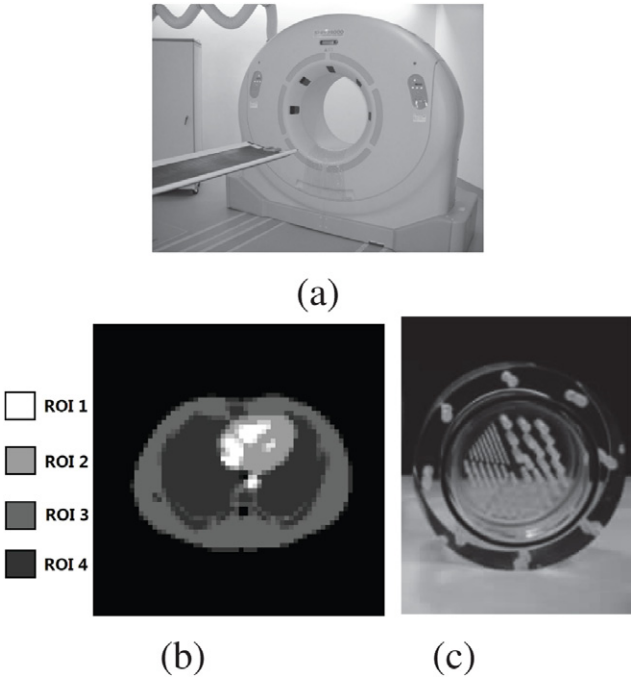


**Figure 3.** (*a*) The gantry of a Hamamatsu SHR74000 PET scanner; (*b*) one sample of emission activity distributions; (*c*) Derenzo phantom.

### *3.1. Monte Carlo simulations of Zubal phantom*

The first data set used for validation is generated by Monte Carlo simulations. Simulations in our study are performed using the toolbox GATE [57]. The simulated PET scanner in our study is a Hamamatsu SHR74000, which is a newly designed full 3D whole body PET/CT scanner from Hamamatsu Photonics KK. The gantry of the PET scanner is shown in figure 3(*a*). The scanner has large fields of view (FOVs): the transaxial FOV is 576 mm, and the axial FOV is 318 mm. The energy window is generally set to 400–650 keV during acquisitions and corresponding simulations to alleviate disturbances of the scatter coincidence events. According to the results of system performance evaluation, the scatter fraction is 38.1% in full 3D acquisition mode. All the physical phenomena from the annihilation of positrons to the interactions between gamma photons and scintillators are completely simulated, the same as real PET data acquisitions in our studies.

The phantom used for simulations is a Zubal thorax phantom [58]; one sample of the activity distributions in the central slice is shown in figure 3(*b*). There are four different kinds of region of interest (ROI): ROI1, heart; ROI2, muscle; ROI3, chest wall; ROI4, lung. Each ROI has a different level of activity concentration. The ratio of activity concentrations at each level during simulation is about 5 : 3 : 2 : 1 in the four regions. (Note that the activity distribution is not exactly uniform in each ROI). The simulated isotope is F18-FDG. The sinogram slice of the simulation output is arranged as 64 bins covering the whole transaxial FOV by 64 angles over 180 degrees. To validate the accuracy of the variance, a total of 500 noisy data sets are simulated independently. For each data set, about 1M counts are collected. Random coincidences are corrected by the online delayed-window method. Besides emission scans, corresponding blank scans and transmission scans are simulated to calculate attenuation coefficients and perform normalization correction. Scatter correction is performed with the software designed for our PET scanner, which is based on the single scatter simulation (SSS) method.

*3.1.1. Activity mean image reconstruction.* The size of the reconstructed activity image is 64 × 64. The images reconstructed from one particular data set by our method are compared with results reconstructed by EM reconstruction. The optimal iteration number for EM reconstruction is determined according to the statistical approach published in [59]. The EM algorithm and corresponding system probability matrix used in our study are from the MATLAB image reconstruction toolbox developed by Professor J Fessler of the University of Michigan. For $H_\infty$ reconstruction, from the descriptions in section 2.4, the convergence of the algorithm is indicated by the $H_\infty$ gain, and the convergent reconstruction results can be obtained when the $H_\infty$ gain goes steadily.

Since experiments in this section are based on Monte Carlo simulations, the ground truths of activity distributions in each experiment can be obtained exactly. In order to compare the reconstruction results quantitatively, the relative root mean squared error (RMSE) is defined for all experiments as

$$\mathrm{RMSE} = \sqrt{\frac{1}{n-1}\sum_{i=1}^{n}\frac{(X_i^{\mathrm{R}}-X_i^{\mathrm{T}})^2}{(X_i^{\mathrm{T}})^2}} \tag{25}$$

where $X_i^{\mathrm{R}}$ is the reconstructed activity concentration in pixel $i$, $X_i^{\mathrm{T}}$ is the ground truth of activity concentration in pixel $i$, and $n$ is the total number of pixels inside the corresponding ROIs.

The results for the reconstruction of the activity maps by the two algorithms are shown in figure 4. Visually, the $H_\infty$-reconstructed image is much smoother than that reconstructed by the EM method. Moreover, the EM reconstructed image seems to experience obvious noise effects, mainly due to the complicated noise property. The image RMSEs calculated between reconstruction results and ground truths are summarized in table 1, where four ROIs are compared separately. The $H_\infty$ method has overall lower RMSEs than the EM method except in ROI1. These figures and results illustrate that the traditional EM method has less capacity to handle noise with unknown statistical *a priori* distribution. The $H_\infty$ reconstruction framework, on the other hand, consistently yields better quality radioactivity estimates. Same conclusions can be drawn from the visual examples of the selected horizontal profiles, as shown in figure 5.

*3.1.2. Variance estimation and analysis.* During the $H_\infty$ solution procedure, the variances are calculated simultaneously along with the activity mean image reconstruction. To validate the calculated variances statistically, activity mean images are first reconstructed from all 500 data sets, and voxelwise ensemble variances are computed as MC simulation results. To get a more quantitative comparison, again, we computed the relative root mean squared errors (RMSEs) of the $H_\infty$

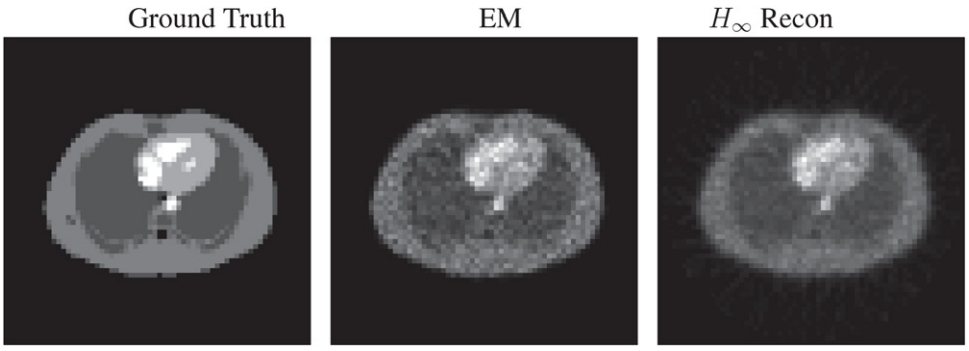


**Figure 4.** The true activity image and reconstructed images by EM and $H_\infty$ algorithm. No post-filtering was applied to the images shown.

**Table 1.** RMSEs of reconstructed images.

| | ROI1 | ROI2 | ROI3 | ROI4 |
|---|---|---|---|---|
| EM | 0.1403 | 0.1711 | 0.2083 | 0.2874 |
| $H_\infty$ | 0.1513 | 0.1537 | 0.1989 | 0.2263 |

method theoretical predictions relative to the MC statistical results for the corresponding ROIs:

$$\mathrm{RMSE} = \sqrt{\frac{1}{n-1}\sum_{i=1}^{n}\frac{(\mathrm{VAR}_i^{\mathrm{R}} - \mathrm{VAR}_i^{\mathrm{MC}})^2}{(\mathrm{VAR}_i^{\mathrm{MC}})^2}} \quad (26)$$

where $\mathrm{VAR}_i^{\mathrm{R}}$ is the $H_\infty$ predicted variance in pixel $i$, and the MC simulation variance $\mathrm{VAR}_i^{\mathrm{MC}}$ is regarded as the ground truth. Besides, the average value of variances in each ROI is also calculated for both the $H_\infty$ predicted variance and the MC statistical variance.

The variance images and corresponding vertical and horizontal profiles through the center for $H_\infty$ and MC statistical methods are shown in figure 6. Both variance images possess an overall distribution similar to that of the mean image, which indicates that variances are strongly dependent on the true activity image. Quantitative comparison between the two methods is shown in table 2. The mean values of variance for the $H_\infty$ method are relatively close to that of the MC results, especially in ROI2 and ROI4. However, the RMSEs in ROI3 and ROI 4 are higher than those in ROI1 and ROI2. Overall, the comparisons show a reasonably good agreement between $H_\infty$ theoretical predictions and the MC statistical results.

### 3.2. Small animal PET scan with Derenzo phantom

The second data set is acquired with a Derenzo phantom using a Concord microPET R4 small animal PET scanner. The microPET R4 is a dedicated scanner for studies of rodents. The transaxial resolution in the center of the FOV is about 1.92 mm according to our recent system performance evaluation. The imaged Derenzo phantom is shown in figure 3(*c*); it consists of six groups of rods with different diameters and different center-to-center spacings. The rod diameters are 1 mm, 1.5 mm, 2 mm, 2.5 mm, 3 mm and 3.5 mm respectively. These experiments illustrate the recovery ability of spatial resolution.

The acquired listmode data are processed to be a sinogram of 96 bins by 96 angles, and random coincidences are corrected by an online delayed-window method. The percentage of random coincidences in the total acquired coincidences is about 2% in this experiment. After normalization correction and Fourier rebinning, the measurement data are reconstructed and the central slice is extracted for illustration. The above processes are finished by programs provided along with the scanner. Generally, attenuation correction and scatter correction are not required in small animal PET imaging.

Figure 7 shows the central slice reconstructed by the two algorithms. The size of the reconstructed central slice is $96 \times 96$. Convergent reconstruction results from the EM algorithm and $H_\infty$ reconstruction are illustrated. As expected, the estimated variance image has an analogous distribution to that of the reconstructed activity map. Since the disturbances from data errors in the small animal PET scan are relatively small, and data corrections and modelings are relatively simple, as the reconstructed images show, they are close to the simulation study. Both algorithms can obtain reasonable results, and rods with 2.5 mm diameter can be distinguished clearly. $H_\infty$ reconstruction can also recover the ROIs well; additionally, the image from $H_\infty$ reconstruction is smoother than that from EM reconstruction.

### 3.3. Real patient scan

The third data set used is a real patient scan acquired with the Hamamatsu SHR-22000 whole body PET scanner located at the Second Affiliated Hospital of Zhejiang University. The SHR-22000 is also designed by Hamamatsu Photonics KK. The scanner has 32 crystal rings, and can be operated in 2D or 3D modes. The recent performance evaluation shows that the transaxial resolution of the central FOV is about 3.7 mm, and more details can be found in [60].

The volunteer patient has a tumor in his left lung. First a 20 min whole body emission scan is performed, then a 20 min transmission scan is followed using rotating $^{68}$Ge rod sources. Finally, a 60 min blank scan (without any radioisotope during acquisition) is performed to calculate the normalization coefficients and attenuation coefficients. The above triple scans are acquired in extended 2D mode, that means data from 63 slices are acquired in all: 32 direct slices plus 31 cross slices between direct slices. The raw sinogram data are 384 bins $\times$ 384 angles, which is reconstructed to images of $96 \times 96$ in our experiments. The random correction, normalization correction, deadtime correction, scatter correction and attenuation correction are performed on the measurement data with the

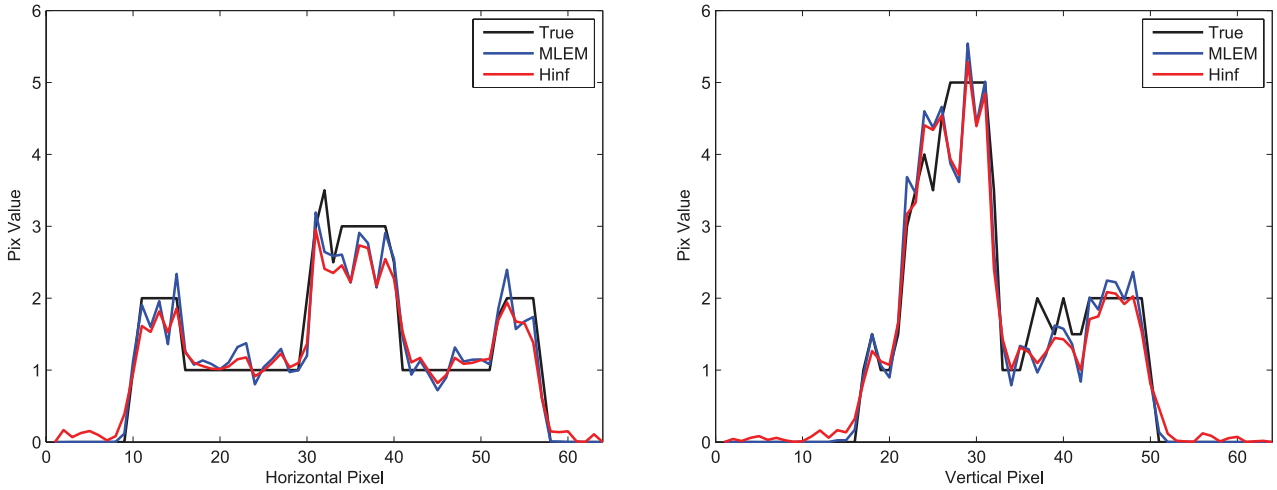


**Figure 5.** The horizontal (left) and vertical (right) profiles through the center of the true image (black), the EM reconstruction (blue) and $H_\infty$ reconstruction (red).

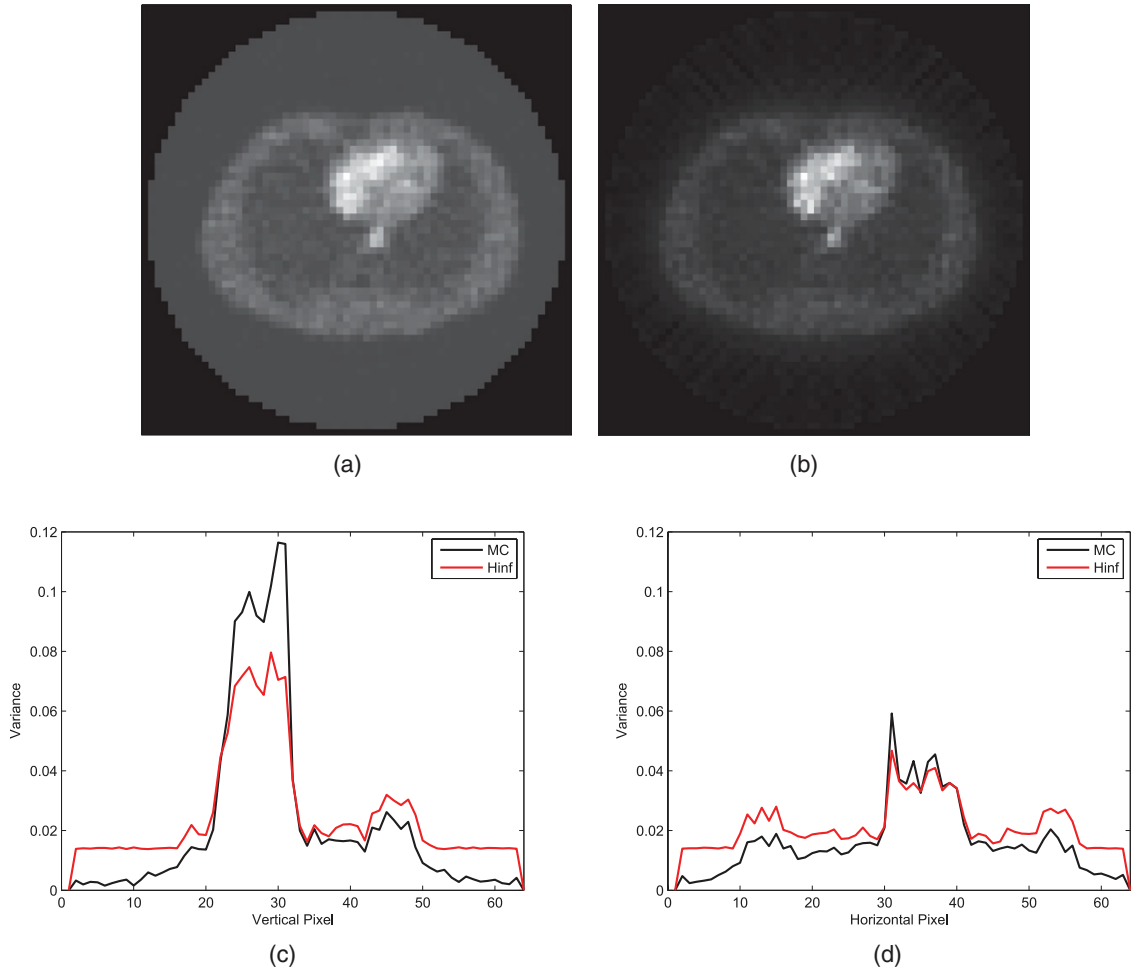


**Figure 6.** Comparison of voxelwise variances: variance images computed (*a*) using the $H_\infty$ method and (*b*) from the 500 reconstructions statistically. (*c*), (*d*) The vertical (*c*) and horizontal (*d*) profiles through the center of (*a*) and (*b*).

**Table 2.** Average values and RMSEs of estimated variances for each ROI.

| | ROI1 | ROI2 | ROI3 | ROI4 |
|---|---|---|---|---|
| Average value of MC | 0.0813 | 0.0441 | 0.0177 | 0.0131 |
| Average value of $H_\infty$ | 0.0662 | 0.0430 | 0.0263 | 0.0186 |
| RMSE | 0.1982 | 0.1181 | 0.5693 | 0.5104 |

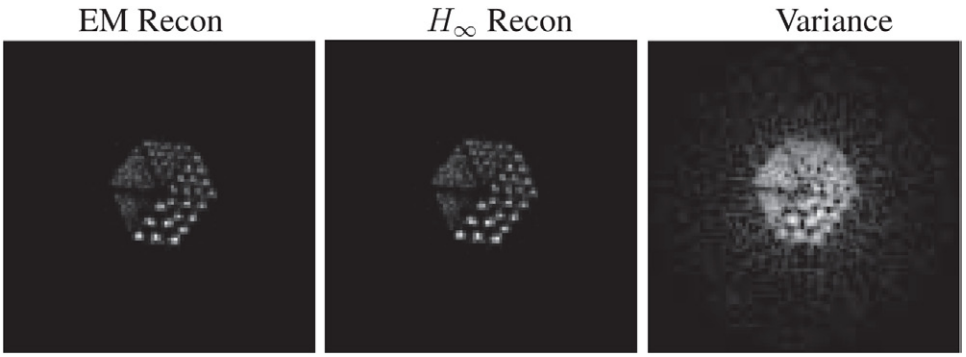


**Figure 7.** Reconstruction results of Derenzo phantom scan by two algorithms.

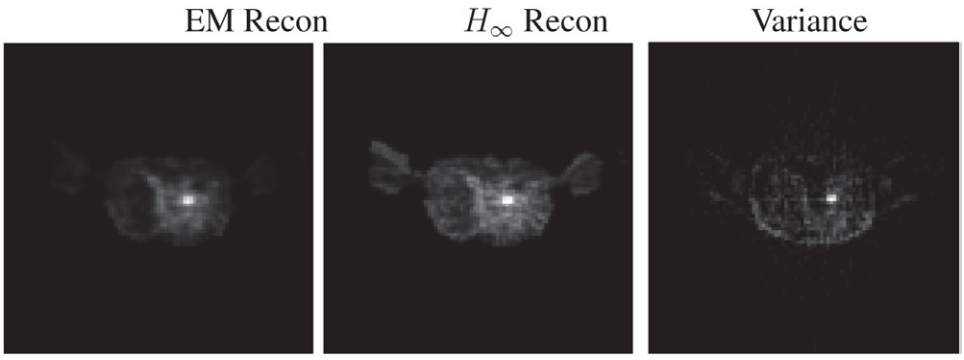


**Figure 8.** Reconstruction results of real patient scan by three algorithms.

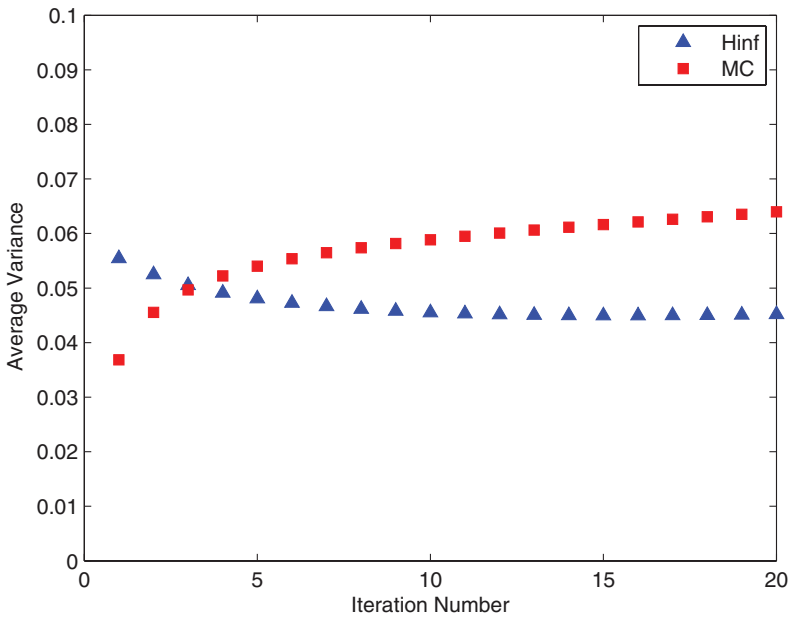


**Figure 9.** Plots of the average variances computed theoretically (triangle marker) and statistically (square marker).

programs provided with the scanner prior to reconstruction. The scatter fraction is about 18% in this extended 2D acquisition mode according to the recent performance evaluation, which is relatively small compared with that of the SHR74000 in full 3D acquisition mode.

These experiments show the reconstruction of real patient data, where completely accurate modelings are not available. The reconstructed images from different algorithms and the estimated variances are shown in figure 8. The activity mean images are Gaussian-smoothed for display. The EM reconstruction can retrieve the tumor region; however, the unavoidable uncertainties during modeling will affect the contrast of the reconstructed images. The $H_\infty$ reconstruction can obtain strong boundaries in reconstructed images and also provide good identification of the tumor. Furthermore, the variance image presented by $H_\infty$ reconstruction also gives us interesting

diagnostic information, namely about the inherent accuracy of the measurement, thus possibly providing confidence for physicians to better diagnose patients.

## 4. Discussion

In this paper, we introduce a minimax criterion, for joint PET mean and variance image estimation, and solve it using an $H_\infty$ filter. The proposed $H_\infty$ framework differs from the previous approaches mainly in the following three aspects: (1) we tackle the estimation problems of the mean and corresponding variance of the radioactivity map simultaneously; (2) no *a priori* knowledge of noise statistics is required; and (3) the min–max estimation criterion is to minimize the worst possible effects of the disturbances (modeling errors and additive noises) on the signal estimation errors, which will ensure that, if the disturbances are small, the estimation errors will be as small as possible. These aspects make the $H_\infty$ framework more robust under any type, and to a lesser extent any level, of noise.

However, in the solution procedure of the $H_\infty$ filter, a matrix inversion is required in every step to calculate the $H_\infty$ gain. Generally, inversion of small matrices is fairly easy, but the inversion of a large matrix will incur more computational costs in a practical implementation. Thus the computational load increases when moving from the EM to the $H_\infty$ filter. One solution is employing the steady state $H_\infty$ filter as a further evolvement of the $H_\infty$ filter, which will achieve significant computational saving with only a little loss of accuracy [61]. Furthermore, this proposed $H_\infty$ filter approach runs efficiently on graphics processing units(GPUs), since large numbers of computations are done in matrix forms. Further investigations on the implementation with GPUs are underway.

PET image reconstruction methods seek to provide 3D or 2D estimated images from measurement data. Since these estimates are functions of noisy data, the noise inevitably propagates and eventually leads to uncertainty in the reconstructed images. We want to emphasize that one of the important concerns in PET imaging is the fact that most reconstruction methods usually provide only the reconstructed images without quantitative metrics representing their quality and reliability, for example, covariance. Given the noise nature of PET measurements, estimating the activity value is not enough to give a complete picture of the measurements. In order to provide more quantitative image reconstructions, covariance information is clearly needed here as well. The proposed $H_\infty$ method realizes joint estimation of both activity value image and covariance information, thus approaching the reconstruction in a complete way. The covariance information may be further used to quantitatively yield an explicit confidence region and even allow calculation of error bars in a straightforward way. Practical applications of such quantitative analysis to designing regularization functions, controlling iteration number and optimizing scanner systems have also been achieved.

Since the PET state space framework is optimized by minimizing the estimation errors, the estimation error covariance $P$ has a general trend of decrement. In contrast, it is commonly acknowledged that the PET image reconstruction is an *ill-conditioned problem*. The amplification effect of data noise and modeling uncertainties on the reconstructed image becomes obvious at large enough iterations. Thus the statistical variance of reconstructions tends to increase with the iteration. To illustrate this discrepancy between theoretical results and statistical results, the average variances of all pixels within the variance images are calculated and plotted as a function of iteration in figure 9. Comparable magnitudes of the two results are limited to only a few iterations. Since large statistical variances indicate a reconstructed image contaminated by noise, it is crucial to terminate iteration early before the reconstructed images become unacceptably noisy.

The weighting matrixes in the objective function are very flexible. When one has accurate models, one can set them to be corresponding covariance matrices of random variables from the models. If one does not have models or one does not want to use the models, one can just simply set them to be identity matrixes. Note that, as introduced in section 2.3, the objective function equation (14) can be extended to dynamic PET image reconstruction. To achieve this application of the minimax framework in dynamic PET reconstruction, one can just substitute equation (10) by the differential equations of predefined kinetic models for dynamic PET imaging.

## 5. Conclusion

We have presented an efficient optimal minimax criterion for joint estimation of the expected activity map and variance distributions in PET imaging. That no *a priori* statistical knowledge assumptions are required makes the minimax criterion robust to both the changes of statistical properties of measurement data after data corrections and uncertainties during system modeling. The framework is optimized with a robust $H_\infty$ filter. Quantitative and qualitative analysis on Monte Carlo simulations validates the performance and accuracy of the joint estimation. Experiments on phantom scans with a small animal PET scanner and real patient scans are also show its clinical potential.

## Acknowledgments

The authors would like to thank staff from the fifth group, Central Research Laboratory, Hamamatsu Photonics KK, for providing help in Monte Carlo simulations and real patient scans.

## References

[1] Wahl R L and Buchanan J W 2002 *Principles and Practice of Positron Emission Tomography* (Baltimore, MD: Williams & Wilkins)
[2] Bailey D, Townsend D, Valk P and Maisey M 2005 *Positron Emission Tomography: Basic Sciences* (New York: Springer)
[3] Valk P, Delbeke D, Bailey D, Townsend D and Maisey M 2006 *Positron Emission Tomography: Clinical Practice* (New York: Springer)
[4] Lewitt R M and Matej S 2003 *Proc. IEEE* **91** 1588–611

[5] Qi J and Leahy R M 2006 *Phys. Med. Biol.* **51** R541–78
[6] Kadrmas D J, Casey M E, Black N F, Hamill J J, Panin V Y and Conti M 2009 *IEEE Trans. Med. Imaging* **28** 523–34
[7] Alessio A M, Kinahan P E and Lewellen T K 2006 *IEEE Trans. Med. Imaging* **25** 828–37
[8] Tsui B, Zhao X, Frey E and Gullberg G 1991 *IEEE Trans. Nucl. Sci.* **38** 1766–72
[9] Kaufman L 1993 *IEEE Trans. Med. Imaging* **12** 200–14
[10] Fessler J 1994 *IEEE Trans. Med. Imaging* **13** 290–300
[11] Lange K and Carson R 1984 *J. Comput. Assist. Tomogr.* **8** 306–16
[12] Nuyts J, Michel C and Dupont P 2001 *IEEE Trans. Med. Imaging* **20** 365–75
[13] Reilhac A, Tomei S, Buvat I, Michel C, Keheren F and Costesa N 2008 *NeuroImage* **39** 359–68
[14] Yavuz M and Fessler J A 1998 *Med. Image Anal.* **2** 369–78
[15] Li Q and Leahy R 2006 *IEEE Trans. Med. Imaging* **25** 1565–72
[16] Chen T B, Chen J C, Lu H H S and Liu R S 2008 *Med. Eng. Phys.* **30** 680–6
[17] Hudson H and Larkin R 1994 *IEEE Trans. Med. Imaging* **13** 601–9
[18] Ming-Kai Y, Shuang-Quan L, Bao-Gi S and Long W 2010 *Chin. Phys.* C **34** 231
[19] Qi J and Leahy R 1999 *IEEE Trans. Med. Imaging* **18** 293–305
[20] Tang J and Rahmim A 2009 *Phys. Med. Biol.* **54** 7063–75
[21] Wang C H, Chen J C and Liu R S 2004 *Comput. Med. Imaging Graph.* **28** 177–84
[22] Mumcuoglu E U, Leahy R M and Cherry S R 1996 *Phys. Med. Biol.* **41** 1777–807
[23] Hebert T and Leahy R 1989 *IEEE Trans. Med. Imaging* **8** 194–202
[24] Tong S, Alessio A M, Kinahan P E, Liu H and Shi P 2011 *Phys. Med. Biol.* **56** 2481
[25] Hoffman E J, Huang S C, Phelps M E and Kuhl D E 1981 *J. Comput. Assist. Tomogr.* **5** 391–400
[26] Ollinger J M 1996 *Phys. Med. Biol.* **41** 153–76
[27] Cherry S R, Sorenson J and Phelps M 2003 *Physics in Nuclear Medicine* (Philadelphia, PA: Saunders)
[28] Zaidi H, Montandon M and Meikle S 2007 *NeuroImage* **34** 518–41
[29] Bendriem B and Townsend D W 1998 *The Theory and Practice of 3D PET* (New York: Kluwer)
[30] Bao Q, Newport D, Chen M, Stout D B and Chatziioannou A F 2009 *J. Nucl. Med.* **50** 401–8
[31] Lewellen T 2008 *Phys. Med. Biol.* **53** R287
[32] Gregory R, Partridge M and Flower M 2006 *IEEE Trans. Nucl. Sci.* **53** 93–101
[33] Teras M, Tolvanen T, Johansson J, Williams J and Knuuti J 2007 *Eur. J. Nucl. Med. Mol. Imaging* **34** 1683–92
[34] Jakoby B, Bercier Y, Watson C, Bendriem B and Townsend D 2009 *IEEE Trans. Nucl. Sci.* **56** 633–9
[35] Yang Y, Wu Y, Qi J, St James S, Du H, Dokhale P, Shah K, Farrell R and Cherry S 2008 *J. Nucl. Med.* **49** 1132
[36] Qi J 2001 *IEEE Trans. Nucl. Sci.* **48** 1470–6
[37] Vunckx K, Bequé D, Defrise M and Nuyts J 2008 *IEEE Trans. Med. Imaging* **27** 36–46
[38] Fessler J A and Rogers W L 1996 *IEEE Trans. Image Process.* **5** 1346–58
[39] Ahn S and Leahy R M 2008 *IEEE Trans. Med. Imaging* **27** 413–24
[40] Huesman R 1984 *Phys. Med. Biol.* **29** 543
[41] Wilson D W and Tsui B M 1993 *IEEE Trans. Nucl. Sci.* **40** 1198–203
[42] Barrett H H, Wilson D W and Tsui B M 1994 *Phys. Med. Biol.* **39** 833
[43] Wang W and Gindi G 1997 *Phys. Med. Biol.* **42** 2215
[44] Soares E J, Byrne C L and Glick S J 2000 *IEEE Trans. Med. Imaging* **19** 261–70
[45] Fessler J A 1996 *IEEE Trans. Image Process.* **5** 493–506
[46] Qi J 2003 *Phys. Med. Biol.* **48** 3505
[47] Li Y 2011 *Phys. Med. Biol.* **56** 1083–103
[48] Glad T and Ljung L 2000 *Control Theory* (London: Taylor and Francis)
[49] Liu H, Tian Y and Shi P 2005 *Information Processing in Medical Imaging* vol 3656 (Berlin: Springer) pp 197–209
[50] Landau I D and Zito G 2006 *Digital Control System: Design, Identification and Implementation* (New York: Springer)
[51] Kwakernaak H 1993 *Automatica* **29** 255–73
[52] van der Schaft A 2000 *L2-Gain and Passivity Techniques in Nonlinear Control* (New York: Springer)
[53] Shen X and Deng L 1997 *IEEE Trans. Signal Process.* **45** 1092–5
[54] Gao F, Liu H and Shi P 2010 *Medical Image Computing and Computer-Assisted Intervention* **3** (Berlin: Springer) p 571
[55] Tong S and Shi P 2007 *Information Processing in Medical Imaging* vol 4584 (Berlin: Springer) pp 421–33
[56] Lim J 2014 *Digit. Signal Process.* **34** 1–5
[57] Jan S *et al* 2004 *Phys. Med. Biol.* **49** 4543–61
[58] Zubal I G, Harrell C R, Smith E O, Rattner Z, Gindi G and Hoffer P B 1994 *Med. Phys.* **21** 299–302
[59] Conti M and Casey M 2007 *Nuclear Science Symp. Conf. Record* vol **6** pp 4389–94
[60] Tian Y, Katabe A, Liu H, Bao C and Yamashita T 2006 *High Energy Phys. Nucl. Phys.* **30** 1123–7
[61] Simon D 2006 *Optimal State Estimation: Kalman, $H_\infty$ and Nonlinear Approaches* (New York: Wiley)